ELSEVIER

Polymer 40 (1999) 4647–4657

polymer

Molecular structure and orientation in processed polymers
2. Application to aromatic polyester fibers

D.C. Oda, G.C. Rutledge*

Department of Chemical Engineering, Massachusetts Institute of Technology, Cambridge, MA 02139, USA

Dedicated to Professor Ronald K. Eby on the occasion of his 70th birthday

Received 12 September 1998; received in revised form 23 December 1998; accepted 28 December 1998

Abstract

We characterize the orientation distribution function (ODF) of molecular-scale structure in a set of solution- and melt-spun fibers of a liquid crystalline polyester in order to assess the role of processing in these fibers. The polyester is composed of 40% 1,4-hydroxybenzoic acid, 30% isophthalic acid, and 30% hydroquinone. Crystallinity is measured by both wide angle X-ray scattering (WAXS) and differential scanning calorimetry (DSC). A three-component model, consisting of crystalline, oriented non-crystalline, and unoriented non-crystalline components, is required to describe completely the X-ray scattering properties of the fibers. Monte Carlo simulations are used to define the ensemble structure on the atomic scale, for which the resulting ODF is determined. Our results indicate that a single ensemble of dimers on a 3×3 rhombic lattice can be used to characterize the molecular-level non-crystalline structure in all the fibers considered. Fibers spun from the nematic melt produce samples with higher degrees of global orientation as well as a higher degree of crystallinity than those spun from solution. Our results also show that the mechanical bias of the fiber spinning process induces an initial degree of orientation which is then enhanced and perfected, especially in the directions lateral to the chain, by subsequent annealing. © 1999 Elsevier Science Ltd. All rights reserved.

Keywords: Wide angle X-ray scattering; Orientation distribution function; Aromatic polyesters

1. Introduction

Aromatic polyesters, or polyarylates, are of interest owing to their favorable physical properties, particularly in high strength, high modulus (HSHM) applications. The HSHM field for polymers has developed rapidly since the commercial introduction of polyaramids such as, Nomex^{tm} (poly(*m*-phenylene isophthalamide)) and Kevlar^{tm} (poly(*p*-phenylene terephthalamide)). These rod-like molecules align in their fluid phase and form liquid crystals (LC). Aligned chains have a tendency to aggregate into larger structures, termed ‘‘domains.’’ When these liquid crystal domains are all mutually aligned, as is the case in fiber spinning, a marked increase in the material’s tensile modulus in the direction of alignment is observed. Once these highly aligned domains are cooled below the melting transition and annealed, crystallinity is induced and the material approaches the theoretical limits of the strengths of the constituent covalent bonds [1–3]. Polyarylates are melt processible alternatives to the solution-processed aramids. One of these is the terpolyester consisting of 1,4-hydroxybenzoic acid (H), isophthalic acid (I), and hydroquinone (Q), termed HIQ-*x*, where *x* denotes the mol% of 1,4-hydroxybenzoic acid in the polymer. The constituents are shown schematically in Fig. 1. As isophthalic acid contains a *m*-phenylene moiety, the linear nature of the polyester backbone is disrupted. However, the polymer chain backbone remains fairly rigid, if not rod-like [4]. HIQ-*x* has been reported to display a liquid crystalline phase when $20 < x < 80$. Additionally, the window of liquid crystallinity is ~ 50°C for HIQ-*x* compositions of $30 < x < 50$ [5,6]. A 50°C range has been reported as the minimum temperature window necessary for viability in industrial processing [5]. For HIQ-*x* fibers, Erdemir et al. proposed an orthorhombic unit cell with $a = 5.58$ Å, $b = 3.92$ Å, and $c = 24.32$ Å ($\rho = 1.49$ g/cm^3) [7]. A similar unit cell was reported by Blundell [5]. The HIQ-*x* powder unit cell has been shown experimentally to be very similar to that of poly(*p*-phenylene isophthalate) (PPI or HIQ-0) [6,8]. Cao and coworkers observed that only a minor shift of axes was required to obtain the monoclinic PPI unit cell from the orthorhombic HIQ-*x* unit cell.

Processing affects a material’s bulk properties, such as

---

* Corresponding author. Tel.: + 1-617-253-0171; fax: + 1-617-258-8224.

E-mail address: rutledge@mit.edu (G.C. Rutledge)

PII: S0032-3861(99)00064-6

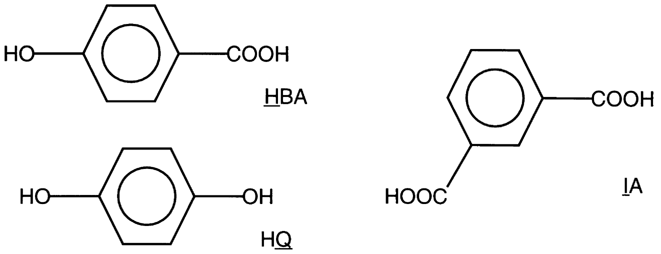

Fig. 1. Schematic of the three constituents of HIQ-*x*: 1,4-hydroxybenzoic acid (HBA), isophthalic acid (IA), and hydroquinone (HQ).

the tensile strength, through changes induced in the molecular-scale morphology and orientation. The orientation in the non-crystalline component of a number of polymers have been studied previously. Bartczak et al. [9] and Galeski et al. [10] investigated uniaxially deformed specimens of both polyethylene and Nylon-6,6 processed in plane strain deformation using wide angle (WAXS) and small angle (SAXS) X-ray scattering techniques. They observed a six-point pattern in their pole figures, indicating that a hexagonal arrangement of chains characterizes the non-crystalline structure for both polymer systems. Mitchell and Windle have investigated poly(methyl methacrylate), PMMA, using WAXS [11,12]. They used an expansion in Legendre polynomials to separate the orientation and structural contributions to WAXS data in PMMA. They modeled the structural contributions using a cylindrical distribution function based on the conformations of short sections of single PMMA chains, concentrating on the intrachain scattering at high scattering vectors. They did not attempt to make direct correlations concerning chain packing. Other groups have studied the crystalline and non-crystalline portions of WAXS patterns from semi-crystalline powders and fibers [13–19]. In each case, the non-crystalline features of the WAXS patterns were characterized using pre-determined peak shapes. For HIQ-*x* polymers, the degree of crystallinity is rarely reported to be above 30% [5], indicating that the non-crystalline component is especially important to the properties of these materials.

Biswas and Blackwell investigated the meridional scattering of X-ray fiber patterns of the liquid crystal random copolymer of 1,4-hydroxybenzoic acid and 2,6-hydroxynaphthaloic acid (trade name: Vectra$^{\mathrm{tm}}$) quite extensively [20–23]. They showed that an aperiodic set of scatterers along the chain backbone can still produce a set of sharp-featured coherent interference patterns. They demonstrated this principle in both experiment and simulation using Vectra$^{\mathrm{tm}}$ as an example.

Molecular-scale analyses of these materials is important in gaining a fundamental understanding of processing-structure-property relationships. As the alignment and packing of chains strongly influence the macroscopic properties, quantifying these features of the solid-state molecular-scale structure is crucial. However, the molecular-scale packing behavior of the non-crystalline phase in many polyarylates is still not very well understood. The non-crystalline component of these materials often accounts for more than half of the material by mass in a given sample. In this study, we use WAXS to measure the molecular-scale orientation and structure in our fiber samples. We look at both the crystalline and non-crystalline components of the WAXS pattern. For the non-crystalline component, a Legendre polynomial series expansion analysis is used to quantify the variation between the members of a set of four HIQ-40 fibers which differ in their processing history.

2. Experimental

Solution- and melt-spun HIQ-40 fibers were provided by Hoechst–Celanese (Summit, New Jersey). The solution-spun fibers were spun from a solution of 20% dichloromethane and 80% trifluoroacetic acid, while the melt-spun fibers were spun from a nematic melt ($T_{\mathrm{c-n}} = 333$°C for HIQ-40) [5]. Bundles of both the melt- and solution-spun HIQ-40 fibers were subsequently thermally annealed at 300°C for 68 h at fixed length. This set of HIQ-40 fiber samples allows comparison of the two separate processing variables: the type of spinning process and the effect of heat treatment. The samples are coded as HIQ40f*ab*, where f indicates fiber sample geometry, *a* indexes the spin process (i.e. *s*olution or *m*elt), and *b* indexes whether or not the samples were annealed (i.e. *a*s-spun or *h*eat-treated).

Optical microscopy was used to measure the outer diameter of the fibers to an accuracy of ± 0.01 μm. Optical micrographs were taken on instant processing film using a Nikon AFX-II photomicrographic attachment on a Nikon Optiphot-pol polarized light microscope. A Perkin–Elmer DSC-7, operated at a scanning rate of 10°C/min, was used to characterize the thermodynamic transitions. The scanning range tested was 100–450°C.

WAXS fiber diagrams of the four fiber samples were obtained using a Rigaku RU 200B rotating copper anode with $\theta/2\theta$ goniometer, a pole figure attachment, and a detector using a proportional intensity photomultiplier. The wavelength of the incident CuK_{α} X-ray radiation was 1.54 Å. The 2D fiber patterns were collected in the azimuthal angle, α, over a range of 0–90° in steps ($\Delta\alpha$) of 4–6°, depending on the sharpness of crystalline features in the fiber. The scattering angle, 2θ, was measured over the

Table 1
HIQ-40 fiber optical microscopy and DSC results. The parenthetical values after the fiber diameter indicate the statistical error estimates. T_{c-n}, onset, and enthalpy values are indicatively of the relative mean, range, and areas of the crystal-to-nematic transition, respectively

	hiq40fsa	hiq40fsh	hiq40fma	hiq40fmh
Fiber diameter (μm)	42.6 (± 0.7)	30.8 (± 0.2)	27.1 (± 0.7)	24.8 (± 0.2)
T_{c-n} (°C)	318	335	318	344
Onset (°C)	290	325	306	335
Enthalpy (J/g)	5.01	24.98	9.01	25.98

range of 10–52° with steps ($\Delta 2\theta$) of 0.1°. The detector was held at each 2θ–α combination for a minimum of 5 s to ensure a reasonable signal to noise ratio.

The crystalline diffraction of a given sample was deconvoluted using 2D Gaussian peak fitting [17–19]. The objective function to be minimized was of the following form:

$$\mathrm{OBJF} = \sum_{2\theta}\sum_{\alpha}(I_{\mathrm{obs}}(2\theta,\alpha) - I_{\mathrm{calc}}(2\theta,\alpha))^2, \tag{1}$$

where

$$I_{\mathrm{calc}}(2\theta,\alpha) = a2\theta + b\alpha + c + \sum_{i=1}^{N_{\mathrm{peaks}}} A_i\, \mathrm{e}^{-\ln 2((2\theta_i-2\theta)/(\omega_{2\theta i}/2))^2}\, \mathrm{e}^{-\ln 2((\alpha_i-\alpha)/(\omega_{\alpha i}/2))^2}. \tag{2}$$

The background for the system was assumed to be linear. Five parameters were fitted for each peak i: the maximum amplitude, A_i; the mean scattering angle, $2\theta_i$; the Full Width at Half Maximum (FWHM) in 2θ, $\omega_{2\theta i}$; the mean azimuthal angle, α_i; and the FWHM in α, $\omega_{\alpha i}$, for a total of $5N_{\mathrm{peaks}} + 3$ degrees of freedom for each sample. In principle, Gaussians are not necessarily justified in the azimuthal direction of α; nevertheless, for the fairly narrow distributions of the crystalline peaks, the use of Gaussians is generally deemed a reasonable approximation. As shown later, some artifacts are introduced using Gaussian peak shapes which might have been mitigated by choice of a different crystalline peak profile [13]. However, resolution of these artifacts is not crucial to the analysis presented here. Solely for the purposes of accurate determination of the crystalline component, up to a total of 4 additional Gaussians were used to approximate the scattering from the non-crystalline regions. Differentiating crystalline and non-crystalline peaks is not trivial. Using the Scherrer equation, a FWHM $\omega_{2\theta i}$ of 5.0° corresponds to a crystallite thickness of ~ 16 Å [24], which exceeds the size of structures used in computer simulation to describe the non-crystalline component. We therefore assumed that peaks with $\omega_{2\theta i} < 5.0°$ belonged to the crystalline component. These peaks were subtracted from the experimental pattern to obtain the contribution from the non-crystalline component. The non-crystalline pattern was then corrected for incoherent (Compton) scatter $I_{\mathrm{comp}}(s)$ and self-scatter, $\Sigma f^2(s)$ and normalized as described in the first paper in this series [25], hereafter referred to as Paper I. The resulting pattern was then analyzed using a Legendre polynomial series expansion in terms of cos α

$$I_{\mathrm{ex},a}(s,\alpha) = \sum_{n=0}^{\infty} A_{2n}(s)P_{2n}(\cos\alpha), \tag{3}$$

where the structure factor coefficient traces, $A_{2n}(s)$, are defined from the orthogonality of the basis functions as:

$$A_{2n}(s) = (4n+1)\int_0^{\pi/2} I_{\mathrm{ex}}(s,\alpha)\cdot P_{2n}(\cos\alpha)\sin\alpha\,\mathrm{d}\alpha. \tag{4}$$

From the series expansion, we obtain a set of scattering coefficient traces, $A_{2n}(s)$. A Monte Carlo simulation was used to generate the theoretical structure factor traces, $A_{2n}^{\mathrm{calc}}(s)$, for an ensemble of oligomers packed on a lattice as described in Paper I [25]. The determination of the proper structural parameters was done iteratively. Initial estimates of the 2D lattice parameters consisted of variations of either a regular hexagonal array or the lateral spacings of the crystalline lattice. As previously noted [25], the isotropic structure factor coefficient, $A_0(s)$, has two contributing factors, oriented and unoriented non-crystalline material. By ‘‘unoriented,’’ here we mean no local alignment of chains, i.e. isotropic. This component contributes only to the isotropic coefficient, $A_0(s)$. The isotropic amorphous trace was determined using commercially available software [26] as described in Paper I [25].

The scaling coefficients, D_{2n}, are determined from the comparison of theoretical calculations to the experimental data

$$A_{2n}(s) = \frac{4n+1}{4\pi}D_{2n}\cdot A_{2n}^{\mathrm{calc}}(s). \tag{5}$$

The D_{2n}'s are then used to reconstruct the orientation distribution function (ODF)

$$D(\alpha) = \sum_{n=0}^{\infty}\frac{4n+1}{4\pi}D_{2n}P_{2n}(\cos\alpha), \tag{6}$$

where

$$2\pi\int_0^{\pi} D(\alpha)\sin\alpha\,\mathrm{d}\alpha = 1. \tag{7}$$

As the distribution being described becomes more narrow, the number of terms (and therefore number of coefficient traces) increases.

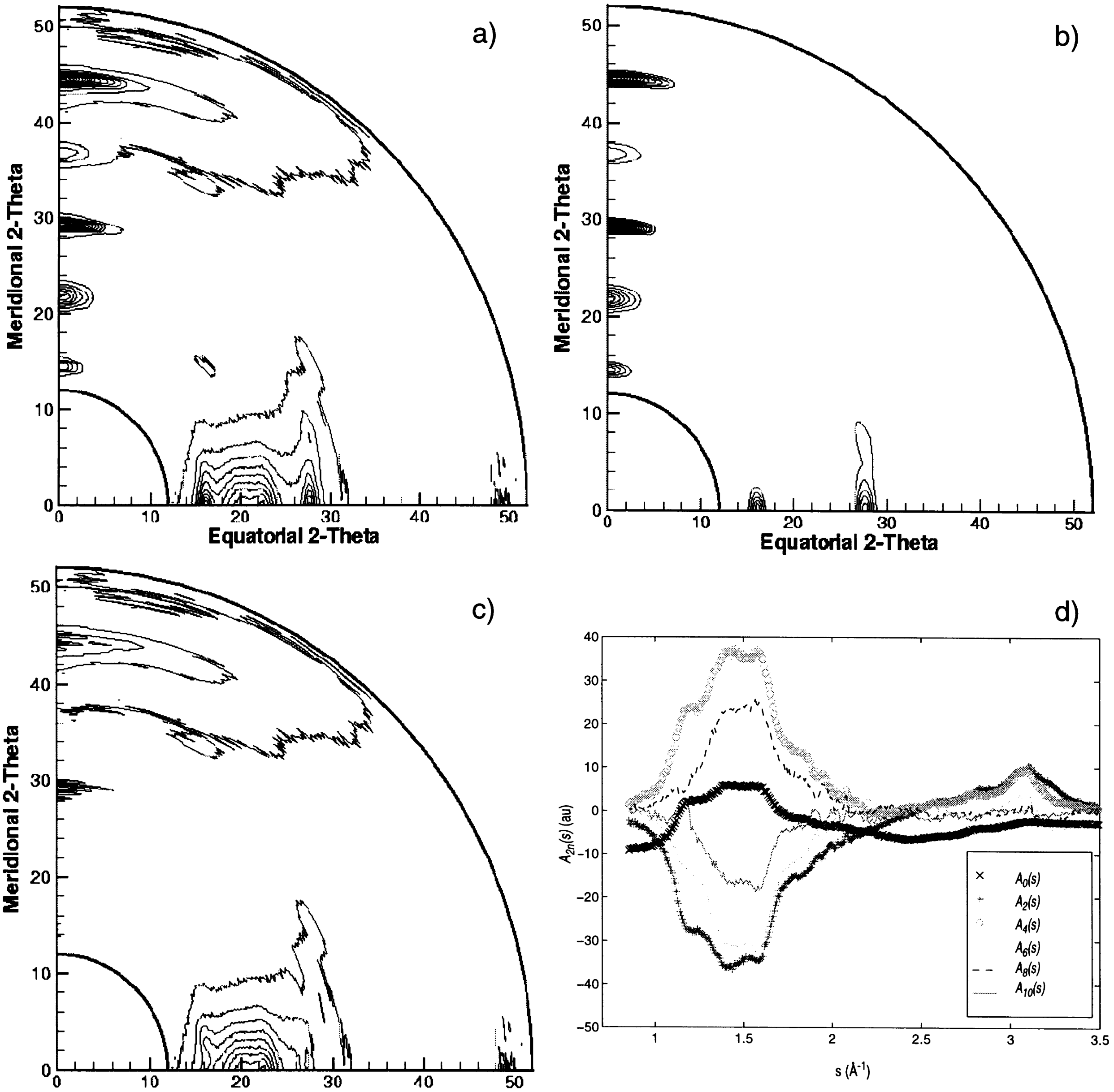

Fig. 2. Fiber Patterns for HIQ-40 annealed melt-spun fiber (hiq40fmh) (a) raw experimental data trace, (b) crystalline component, (c) non-crystalline component, (d) experimental coefficient traces, $A_{2n}(s)$, from the Legendre polynomial series expansion. Only up to $2n = 10$ is included for clarity.

3. Results and discussion

3.1. Calorimetry and optical microscopy

Table 1 summarizes the optical microscopy and differential scanning calorimetry (DSC) results for the four fiber samples, listing the fiber diameters and the associated error; the melting peak maximum temperature, T_{c-n}; the melting peak onset, which is a reflection of the breadth of the distribution; and integrated area under the peak or melting enthalpy, ΔH_f. T_{c-n} for the as-spun fiber samples is lower than that reported for the powder (333°C), while the heat-treated fibers display T_{c-n}'s comparable to the reported literature data. This suggests that either the degree of crystal perfection is lower in the as-spun samples or the breadth of the distribution of crystallite sizes is higher. Likewise, the broader melting peak ranges for the as-spun samples compared to the heat-treated fibers suggest similar conclusions. To our knowledge, there is no reported value for the heat of fusion, ΔH_f^0, for HIQ-*x* crystallites. Therefore, DSC provided only relative measures of crystallinity in this case. Our results indicate that the degree of crystallinity increases 300–500% during annealing, for both solution- and melt-spun fibers. Erdemir et al. note that as-spun melt fibers of HIQ-*x* display a very broad endotherm in the temperature ranges that we observed [6]. From optical microscopy, we

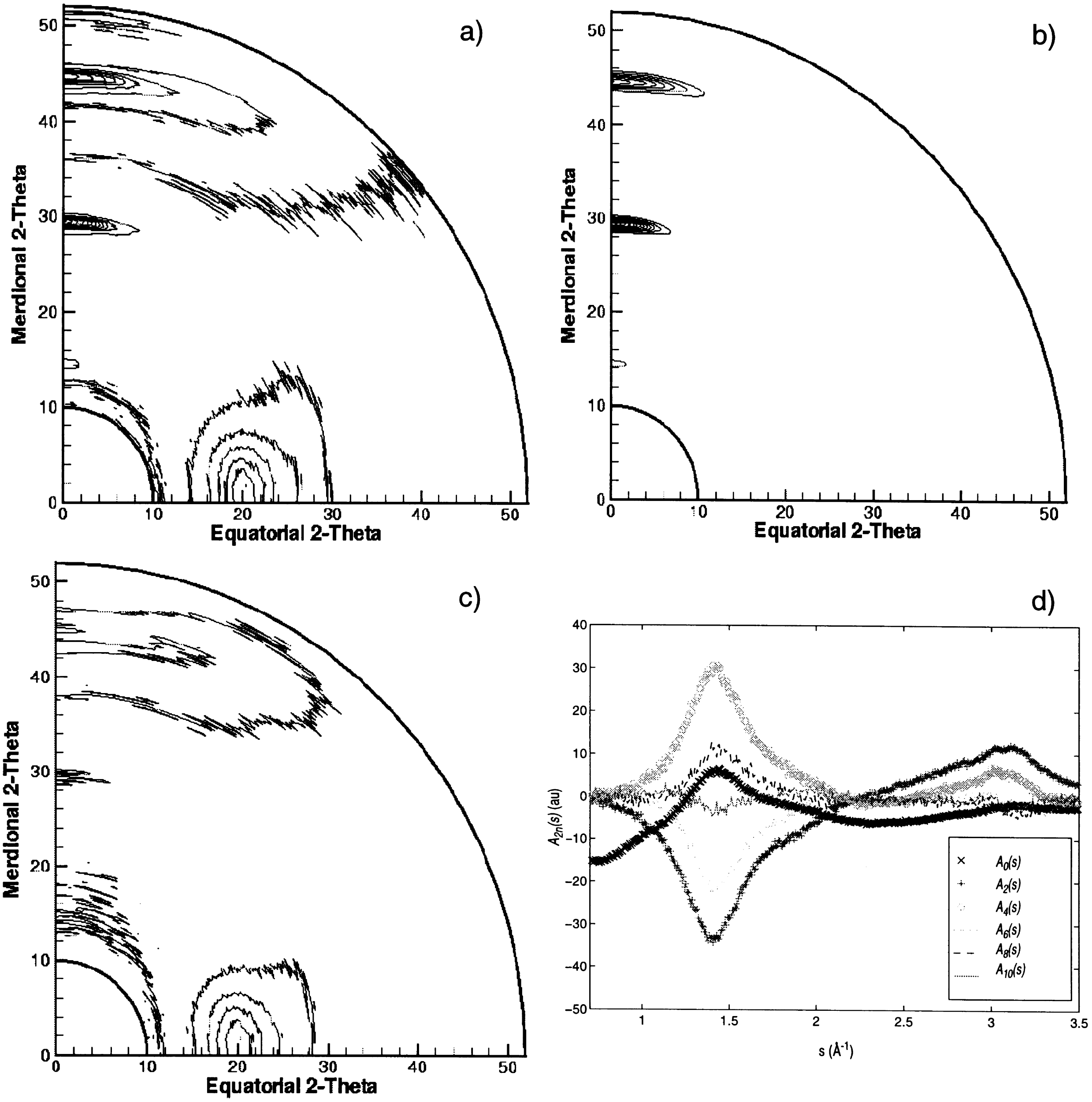

Fig. 3. Fiber Patterns for HIQ-40 as-spun melt-spun fiber (hiq40fma) (a) raw experimental data trace, (b) crystalline component, (c) non-crystalline component, (d) experimental coefficient traces, $A_{2n}(s)$, from the Legendre polynomial series expansion. Only up to $2n = 10$ is included for clarity.

noted that on the fiber surface, there was discoloration and flaking consistent with superficial oxidative degradation of the polymer at 300°C.

3.2. X-ray scattering

Figs. 2–4 show the results of the X-ray analysis involving crystalline deconvolution and series expansion analyses applied to three of the fiber samples; results for the fourth sample in this series are shown in Fig. 2 of Paper I [25]. Part (a) shows the raw experimental data; part (b) shows the crystalline contribution deduced by Gaussian peak fitting; part (c) shows the non-crystalline fraction obtained by subtraction of (b) from (a); and part (d) shows the scattering coefficient traces obtained by decomposition of (c) in a Legendre polynomial series expansion according to Eq. (3).

Table 2 lists the positions of the crystalline peaks deduced by the Gaussian fitting for each of the first three HIQ-*x* fiber samples. The fourth sample, hiq40fsa, exhibits no crystallinity. In every case, the observed peaks could be indexed based on the unit cell proposed by Johnson and coworkers [27–29]. One can see from Table 2 that very few crystalline peaks are observed. This is common for these materials, where degrees of crystallinity as measured by WAXS are generally reported to be less than 30% [5]. The WAXS results indicate crystallinities between 0 and 28% (c.f

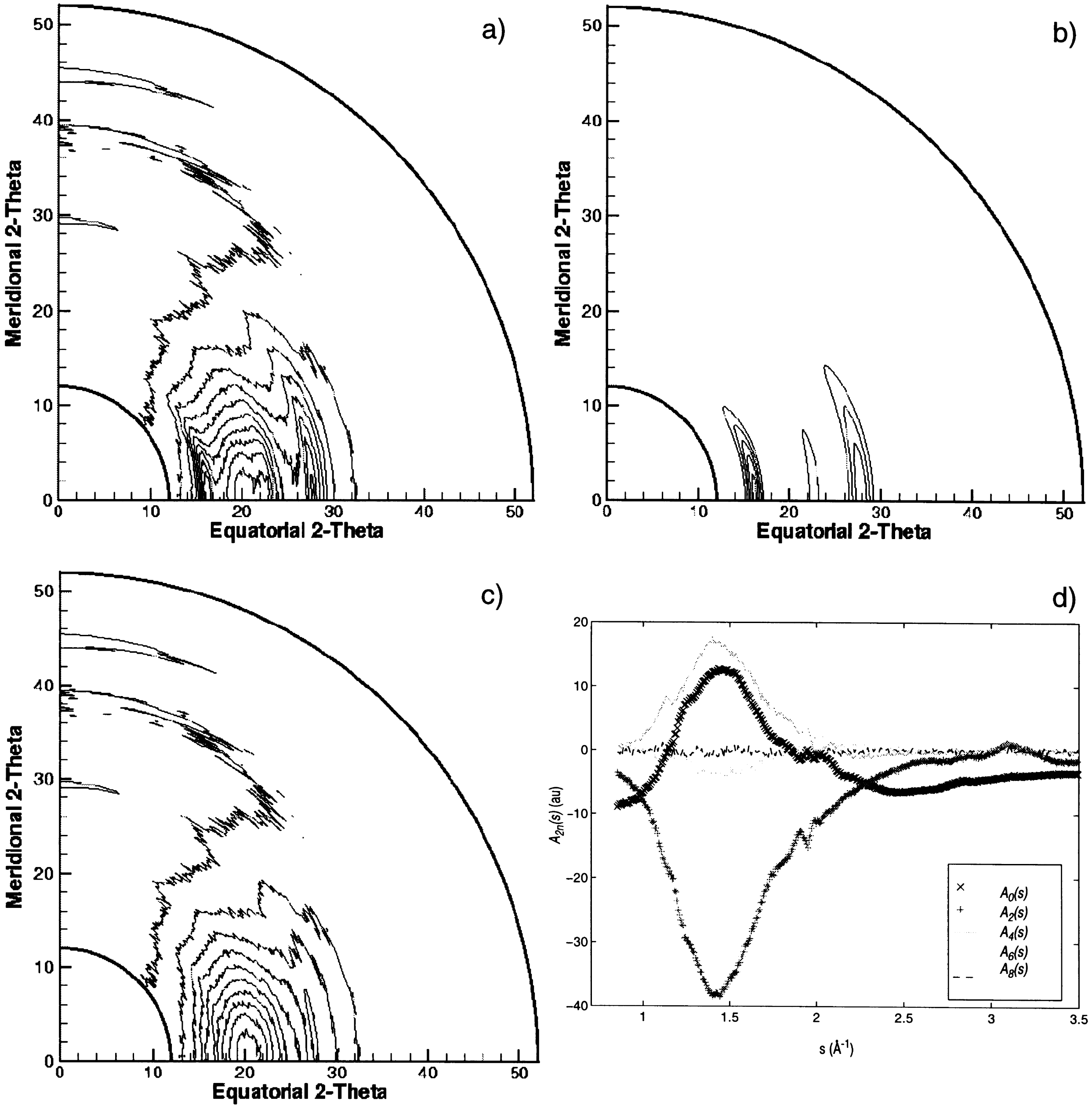

Fig. 4. Fiber Patterns for HIQ-40 annealed solution-spun fiber (hiq40fsh) (a) raw experimental data trace, (b) crystalline component, (c) non-crystalline component, (d) experimental coefficient traces, $A_{2n}(s)$, from the Legendre polynomial series expansion.

Table 4). The hiq40fsh sample displays crystallites with the largest dimensions lateral to the chain, as evidenced by sharpening of the (100), (010), and (110) peaks. In contrast, the hiq40fma fiber pattern displays the sharpest crystalline peaks along the meridian, as evidenced by the sharp (004), (008) and (0012) peaks. Only the hiq40fmh fiber pattern displays significant 3D crystalline order. These results suggest that an extended chain conformation, implied by the meridional peaks, is favored by processing from the nematic melt. In contrast, heat treatment perfects the intermolecular packing of the chains. Also from Table 2, we note that the equatorial crystalline peaks for hiq40fsh have an average azimuthal FWHM, $\langle \omega_{\alpha i} \rangle$, of 47.5°. The equatorial peaks for the hiq40fmh fibers display an $\langle \omega_{\alpha i} \rangle$, of 10.7° and the meridional peaks have an $\langle \omega_{\alpha i} \rangle$, of 10.0°. The meridional peaks of the hiq40fma fibers display an $\langle \omega_{\alpha i} \rangle$, of 14.4°. Comparison of these $\langle \omega_{\alpha i} \rangle$, values indicates two trends: (1) the heat-treated samples display a slightly higher degree of crystalline orientation and (2) the crystalline peaks in the melt-spun fibers display higher degrees of orientation than their solution-spun counterparts.

As can be noted from Table 3, both WAXS and DSC confirm that heat-treatment causes a marked increase in the amount of crystalline material present, more than the processing change of solution- to melt-spinning. In addition, the decrease in FWHM for the crystalline peaks in WAXS

Table 2
HIQ-40 fiber crystalline peak deconvolution results. All values for 2θ, $2\theta_i$, α_i, $\omega_{2\theta i}$, and $\omega_{\alpha i}$ are in degrees. The parenthetical values after each mean value is the FWHM for that spatial direction

Miller index	Reported 2θ	hiq40fsh $2\theta_i(\omega_{2\theta i})$	hiq40fsh $\alpha_i(\omega_{\alpha i})$	Hiq40fma $2\theta_i(\omega_{2\theta i})$	hiq40fma $\alpha_i(\omega_{\alpha i})$	hiq40fmh $2\theta_i(\omega_{2\theta i})$	hiq40fmh $\alpha_i(\omega_{\alpha i})$
004	14.5	—	—	14.5(0.9)	0.4(15.4)	14.5(1.0)	− 0.1(12.9)
100	16.4	16.1(1.2)	89.3(47.3)	—	—	16.1(1.2)	90.0(9.6)
102	17.8	—	—	—	—	17.6(4.1)	88.7(35.7)
010	21.7	22.7(1.3)	91.8(48.0)	—	—	21.4(4.6)	90.2(13.6)
006	21.9	—	—	—	—	21.8(1.7)	− 0.1(10.6)
104	22.5	—	—	—	—	21.8(2.2)	47.3(11.7)
110	27.7	27.9(1.8)	92.8(47.3)	—	—	27.7(1.5)	90.1(9.0)
112	29.4	—	—	—	—	28.5(1.8)	75.9(12.4)
008	29.4	29.4(0.8)	− 3.2(28.1)	29.4(0.9)	0.0(12.6)	29.3(0.9)	− 0.1(9.5)
116	33.1	—	—	—	—	30.6(4.1)	60.8(17.1)
0010	37.0	—	—	—	—	36.8(1.7)	0.0(8.7)
0012*a*	44.5	—	—	44.6(1.3)	0.0(15.1)	44.1(2.2)	− 0.9(27.0)
0012*b*	44.5	—	—	—	—	44.6(0.9)	0.0(8.2)

suggests that annealing also increases crystal size. The melt-spun fibers display a higher initial degree of crystallinity as well as a higher maximum degree of crystallinity. The presence of a melting endotherm in the hiq40fsa samples, where no crystallinity is measured by WAXS, is likely due to the melting of locally ordered regions or small defective crystals. Similar conclusions were drawn by Erdemir and coworkers on HIQ-*x* fibers [7]. If the thermal transition in the fiber sample is due to the local alignment of chains, then the resultant diffuse scattering from the material should be observable by WAXS. The Legendre polynomial series expansion analysis is particularly well suited for the purpose of examining moderately oriented, but diffuse scattering.

While the increased crystallinity in the annealed fibers is not surprising, our results suggest that the amorphous material about the crystallites must also be undergoing a certain amount of structural reorientation. The non-crystalline portions of the WAXS fiber patterns show narrower diffuse scattering features for the annealed samples than for their as-spun counterparts. This suggests that a narrower ODF will be necessary to characterize the samples and their molecular arrangements within these materials. The non-crystalline scattering patterns in Figs. 2–4 part(c) and in Fig. 2(a) from Paper I [25] are similar in a number of respects. There is a broad equatorial peak at $2\theta = \sim 20^\circ$. This diffuse scattered intensity is because of the wide variations of the lateral interchain distance. Sharp peaks along the meridian of the fiber diagram are indicative of extended chain conformations, especially in the melt-spun fibers.

Fig. 5 compares the first four experimental coefficient traces for the HIQ-40 fiber samples. There appear to be two distinct features: an asymmetric peak on the equator near $s = 1.45$ Å^{-1} ($\sim 2\theta = 20^\circ$) and a second peak on the meridian near $s = 3.1$ Å^{-1}. The equatorial feature is an interchain peak and is due to scattering lateral to the chain direction. The meridional feature is considered as an intrachain peak, as it reflects scattering parallel to the fiber axis which is associated with the polymer chain axis. The relative contributions of each trace to the series expansion varies, but the similarity between the shapes of coefficient traces implies that the same molecular ensemble for the theoretical structure factor calculations will apply to each of the samples.

The coefficient traces for the hiq40fmh fibers shown in Fig. 5 are somewhat noisier than the others. This is because of two factors. First, the use of Gaussian peak shapes to analyze the crystalline component is only an approximation; upon subtraction, misfit in the tails of the Gaussian lineshapes leads to shoulders in the non-crystalline scattering. Second, the high degree of crystallinity in hiq40fmh results in a lower signal to noise ratio in the non-crystalline scattering, as none of the noise is taken up in the crystalline scattering. As a result, the coefficient traces, $A_{2n}(s)$, for hiq40fmh are also noisier.

3.3. Modeling

The similar experimental coefficient traces for the HIQ-40 fibers suggest that a single structural ensemble may suffice to describe the molecular-scale structure for all four fiber samples. We used the molecular ensemble derived for the hiq40fsa sample and reported in Paper I [25] for this iso-structural analysis. Using the same model for the non-crystalline structure permits direct comparison of ODFs

Table 3
Scaling coefficients for HIQ-40 fibers in the iso-structural ensemble analysis

	hiq40fsa	hiq40fsh	hiq40fma	hiq40fmh
D_0	1	1	1	1
D_2	0.02	0.10	0.10	0.11
D_4	0.003	0.02	0.04	0.06
D_6	0.001	0.004	0.02	0.04
D_8	—	0.001	0.01	0.02
D_{10}	—	—	0.002	0.01
D_{12}	—	—	0.001	0.006
D_{14}	—	—	—	0.004
D_{16}	—	—	—	0.001

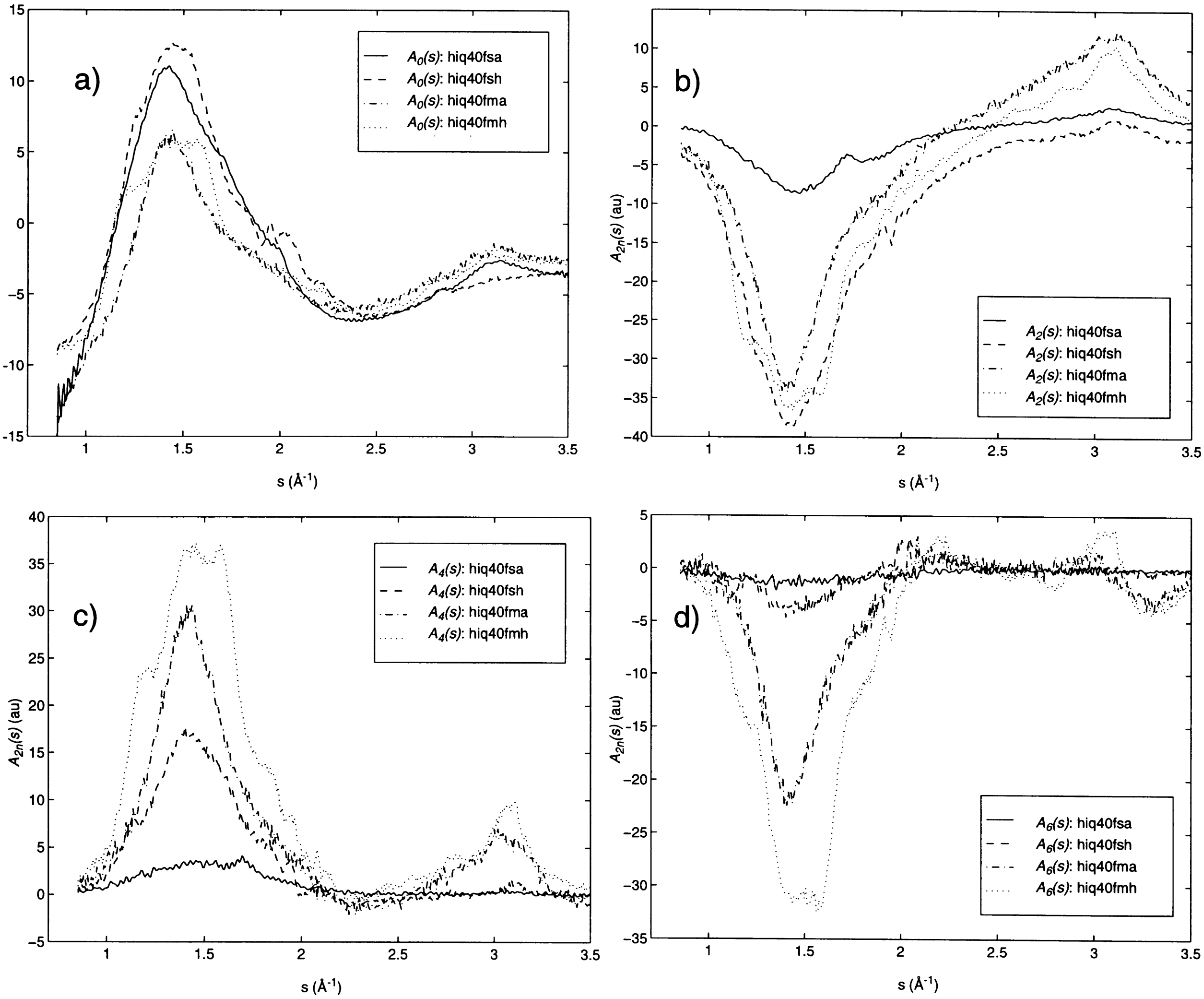

Fig. 5. Comparison of the experimental coefficient traces, $A_{2n}(s)$ ($2n = 0$, 2, 4, and 6), for the four HIQ-40 fiber samples.

between samples, as the molecular model and ensemble parameters influence only peak positions and shape in the $A_{2n}^{\text{calc}}(s)$'s. Thus, the scaling factors, D_{2n}, reflect the orientation of this particular ensemble of structures. The sum of squared deviations between the experimental and calculated traces (a function of χ^2) measures the accuracy with which the model ensemble describes the molecular-scale structure of the sample. Each structure of the model ensemble consists of HIQ-40 dimers on a 3 × 3 lattice with lattice parameters $a = 4.25$ Å, $b = 3.75$ Å, and $\gamma = 80°$. The center of mass of individual chains were permitted to deviate from their lattice sites by as much as $\Delta a = a/2$ and $\Delta b = b/2$. A Monte Carlo procedure was used to sample structures in the ensemble according to the probability

$$p_i \propto \exp(-\beta_T E_i - \beta_\chi \chi_i^2). \qquad (8)$$

A hard sphere potential was used to compute E_i. χ_i^2 represents a weighting function which biases selection in favor of those structures which improve the agreement between the theoretical and observed structure factors; its introduction serves to give preference to those members of the thermodynamic equilibrium ensemble which are selected for during processing, as judged by accordance with the experimentally observed WAXS scattering. The choice of β_χ is at least in part a matter of practicality, within reasonable bounds as described in Paper I [25]; in this work, a value of 1.2×10^{-3} has been used, representing a fairly weak bias. The first four ($n = 0 - 3$) simulated coefficient traces, $A_{2n}^{\text{calc}}(s)$ for the ensemble are shown in Fig. 3 of Paper I. Scaling $A_{2n}^{\text{calc}}(s)$ for the other fibers to get the best agreement with the experimental traces (shown in Fig. 5 up to $n = 3$) yields values of D_{2n} up to $n = 8$ (Table 4). The resulting ODFs obtained by application of Eq. (6) are shown in Fig. 6Fig. 6 . Even though we have very similar local scale structures, the relative contributions to the ODF from the individual coefficient traces varies.

Table 3 contains a breakdown of the percentages of the three components used to characterize the fibers: crystalline, oriented non-crystalline, and unoriented non-crystalline. All

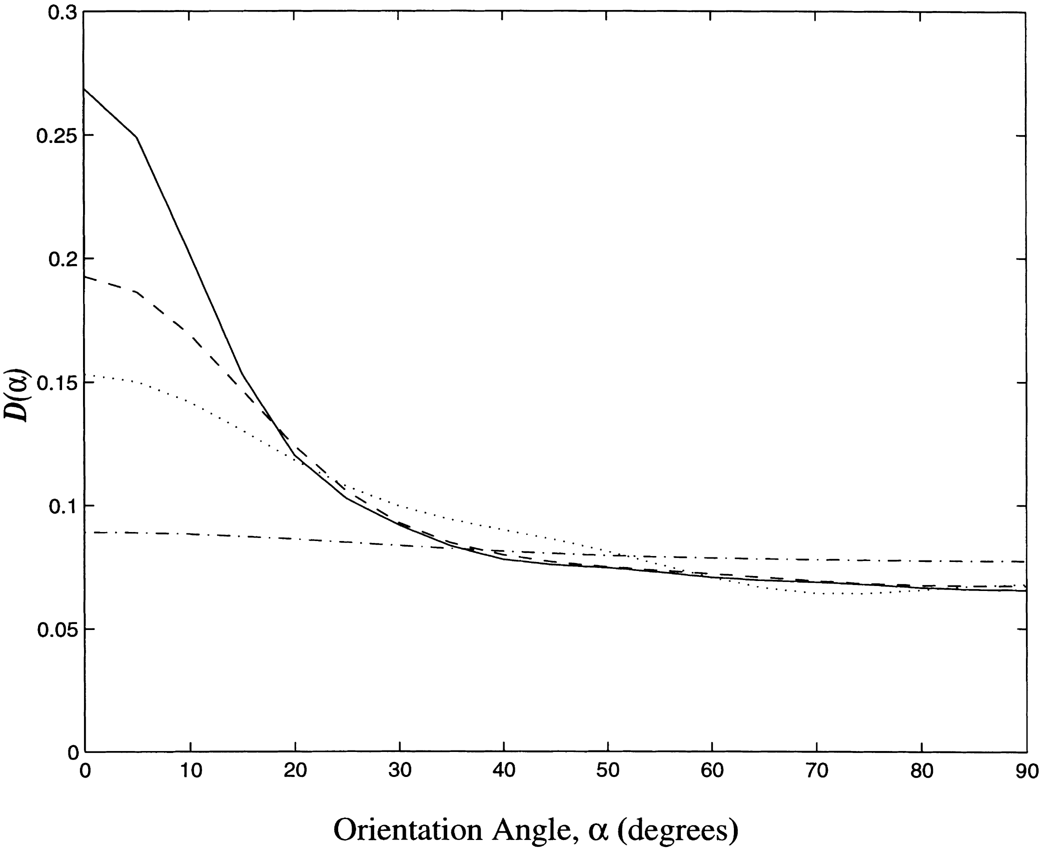

Fig. 6. ODF's for the oriented non-crystalline component of the four HIQ-40 fiber samples in the iso-structural ensemble analysis. Hiq40fmh, solid line (—); hiq40fma, the dashed line (– – –); hiq40fsh, the dotted line (· · ·); and hiq40fsa, the alternating dash–dot line (·–·–·).

three components are well documented in the literature [15,30–34]. While some of the oriented non-crystalline material could be the interfacial material between the crystalline and amorphous components, the relative amount of oriented non-crystalline material (e.g. in hiq40fma over 85% of the chains in the fiber are oriented, while less than 10% are in the crystalline component) and the fact that hiq40fsa fibers contain oriented non-crystalline, but no crystalline material, indicates that the oriented material cannot be assigned exclusively to material constrained to reside at the interface between crystalline and amorphous components.

From Fig. 6, we can see that the melt-spun fibers display a higher degree of orientation than the solution-spun fibers and that the heat-treated specimens display a higher degree of orientation than their unannealed counterparts. However, all of the ODFs show a significant proportion of globally unoriented, but locally aligned material. This confirms that local chain alignment can exist in the absence of a significant level of global orientation. More specifically, upon heat-treating, HIQ-40 fibers exhibit a loss of oriented non-crystalline component, a gain in crystalline component, and little change in unoriented non-crystalline component, regardless of whether the fibers were spun from solution or melt. The ratio of crystalline material produced to oriented non-crystalline material consumed is near unity, suggesting that the crystalline component is generated primarily from the oriented non-crystalline component. This seems to offer quantitative confirmation for the view that heat-treating serves primarily to crystallize previously

Table 4
Orientational structural parameters for HIQ-40 Fibers. The %XTAL, %ONC, and %UNC are the relative fractions of the crystalline, oriented non-crystalline and unoriented non-crystalline material in the whole sample, respectively. The parenthetical numbers after the component fractions are the error ranges associated with the values

	hiq40fsa	hiq40fsh	hiq40fma	hiq40fmh
%XTAL	0.0% (± 0.0%)	18.2% (± 4.0%)	9.2% (± 6.5%)	27.6% (± 5.4%)
%ONC	85.6% (± 10.0%)	66.8% (± 8.2%)	88.0% (± 9.1%)	64.4% (± 7.2%)
%UNC	14.4% (± 10.0%)	15.0% (± 8.2%)	2.8% (± 9.1%)	8.0% (± 7.2%)

aligned chains. It is well established in the literature that the aligned chains crystallize more rapidly than their unoriented counterparts [35–37]. From the FWHM of the ODF peaks, we can see that annealing only causes a slight increase in the degree of global orientation of the aligned chain structures. The effect is smaller in the solution-spun fibers, which we attribute to the fact that the enhancement of alignment between structures and elimination of molecular-scale defects occurs on a smaller size scale in such materials. Heat-treatment of the melt-spun fibers produces a larger decrease in the FWHM of their ODF than heat-treatment of the solution-spun fibers, owing to the fact that the melt-spun fibers are spun from a nematic melt which contains readily oriented domains. The lack of meridional peaks, coupled with the relatively large FWHM of the solution-spun fibers, suggests that the solution-spinning process does not extend the chain conformation, nor does it align the polymer chain segments with respect to each other. The high degree of orientation in the melt-spun fibers is attributed to the presence (and orientation under mechanical bias) of nematic domains in the liquid crystalline phase of the melt from which the fibers were spun. Thus, the spinning process must induce the initial global orientation in the material.

4. Conclusions

We conclude that the melt-spun fibers contain a higher degree of global structural orientation, as evidenced by the narrow azimuthal breadth, and a higher degree of chain extension, as evidenced by the narrow breadth ($\omega_{2\theta i}$) of the meridional crystalline peaks in the hiq40fma and hiq40fmh fibers. The effect of the melt spinning is to induce extended chain conformations and orient the structures containing these extended (and aligned) chains, resulting in a higher degree of orientation in fibers produced by that route. The annealed samples (hiq40fsh and hiq40fmh) display a higher degree of periodicity in directions lateral to the chains, implying that crystallization is more facile in these directions. We envision the chain direction to be somewhat constrained conformationally due to the backbone connectivity; in contrast, the directions lateral to the chain are less constrained by such connectivity.

Our results show that both spinning and heat-treatment lead to greater chain alignment and orientation on the molecular-scale. Annealing has the function of eliminating defects and creating a higher degree of crystalline perfection in the fiber samples. The increased degree of perfection is primarily associated with directions lateral to the chain, whether the chain is in an extended conformation or not. This conclusion is based on the observation that equatorial peaks appear in both annealed fiber samples, but only slight enhancement of meridional peaks is seen in the annealed samples. The annealed samples also show higher degree of crystallinity and orientation of chains in both crystalline and non-crystalline components. Thus, the role of mechanical and thermal processing may be summarized as follows. The mechanical bias from the spinning process establishes the initial orientation of the chains; during annealing, aligned chains in the oriented non-crystalline component of the material are consumed, preferentially over the unoriented non-crystalline component, to support the growth of the crystalline phase. Annealing can perfect partial orientation of chains, but it does not initiate local alignment of them. The comparison of the solution-spun fibers from an isotropic solution and the melt-spun fiber from the nematic melt highlight this fact; the hiq40fsa fibers show little global orientation, whereas the hiq40fma fibers display measurable amounts of global orientation. This degree of orientation is then built upon by the subsequent annealing step.

We performed molecular simulations which generated a structural ensemble. In turn, this ensemble permitted quantitative characterization of the molecular structure and orientation in these fibers and afforded us insight into the relative effects of various processing parameters on the molecular-scale structure of the HIQ-40 fiber samples. Based upon the similarity found in the $A_{2n}(s)$'s, we deduced that the local-scale structures contained within this set of fibers are very similar. We obtained quantitative measures of the fractions of the three components in our samples. The large fraction of oriented non-crystalline component suggests that there is a significant portion of locally aligned material. However, the significant isotropic component, $A_0(s)$, of the oriented non-crystalline ODFs suggests that local alignment between chains does not imply global orientation of these regions of locally aligned chains. The isotropic contribution, $A_0(s)$, to the oriented non-crystalline component is distinct from the unoriented non-crystalline component. The former is locally aligned, but globally unoriented, while the latter displays neither local chain alignment nor global orientation.

Acknowledgements

We are grateful to Dr. M. Jaffe for making the fibers samples of HIQ available for this work. Financial support was provided by the National Science Foundation, award #CTS-9457111. Use of the Perkin–Elmer DSC-7 was made possible by the Center for Material Science and Engineering at MIT, with the support of the National Science Foundation under Award Number DMR-9400334.

References

[1] Rutledge GC. PhD Thesis, Massachusetts Institute of Technology, 1990.
[2] Noel C. In: Chapoy LL, editor. Recent advances in liquid crystalline polymers, London: Elsevier Applied Science, 1985. p. 135.
[3] Ciferri A. Liquid crystallinity in polymers: principles and fundamental properties. New York: VCH, 1991.
[4] Rutledge GC. Macromolecules 1992;25:3984.

[5] Blundell DJ, MacDonald WA, Chivers RA. High Performance Polym 1989;1:97.
[6] Erdemir AB, Johnson DJ, Tomka JG. Polymer 1986;27:441.
[7] Erdemir AB, Johnson DJ, Karacan I, Tomka JG. Polymer 1988;29:597.
[8] Cao J, Karacan I, Tomka JG. Polymer 1995;36:2133.
[9] Bartzcak Z, Cohen RE, Argon AS. Macromolecules 1992;25:4672.
[10] Galeski A, Argon AS, Cohen RE. Macromolecules 1988;21:2761.
[11] Mitchell GR, Windle AH. Colloid Polym Sci 1982;260:754.
[12] Mitchell GR, Windle AH. Colloid Polym Sci 1985;263:230.
[13] Murthy NS, Minor H, Bednarczyk C, Krimm S. Macromolecules 1993;26:1712.
[14] Murthy NS, Zero K, Minor H. Macromolecules 1994;27:1484.
[15] Fu Y, Busing WR, Jin Y, Affholter KA, Wunderlich B. Macromolecules 1993;26:2187.
[16] Fu Y, Annis B, Boller A, Jin Y, Wunderlich B. J Polym Sci Pol Phys 1994;32:2289.
[17] Fu Y, Busing W, Jin Y, Affholter KA, Wunderlich B. Macromol Chem Phys 1994;195:803.
[18] Iannelli P. Macromolecules 1993;26:2303.
[19] Iannelli P. Macromolecules 1993;26:2309.
[20] Biswas A, Blackwell J. Macromolecules 1988;21:3146.
[21] Biswas A, Blackwell J. Macromolecules 1988;21:3152.
[22] Biswas A, Blackwell J. Macromolecules 1988;21:3158.
[23] Blackwell J, Biswas A. Macromolecules 1985;18:2126.
[24] Guinier A. X-ray diffraction in crystals, imperfect crystals and amorphous bodies. New York: Dover, 1963.
[25] Oda DC, Rutledge GC. Polymer 1999;40:4635.
[26] Biosym^{tm} version 2.3.6, available through Molecular Simulations Inc., 9685 Scranton Road, San Diego, CA 92121, 1994.
[27] Johnson DJ, Karacan I, Tomka JG. Polymer 1990;31:8.
[28] Johnson DJ, Karacan I, Tomka JG. J Text Inst 1990;81:421.
[29] Johnson DJ, Karacan I, Tomka JG. Polymer 1992;33:983.
[30] Hristov HA. Barton Jr, R., Schultz, J.M. J Polym Sci Pol Phys 1991;29:883.
[31] Galeski A, Argon AS, Cohen RE. Macromolecules 1992;25:5705.
[32] Fischer EW, Fakirov S. J Mater Sci 1976;11:1041.
[33] Clauss B, Salem DR. Macromolecules 1995;28:8328.
[34] Asano T, Seto T. Polym J 1973;5:72.
[35] Mandelkern L. Crystallization of polymers. New York: McGraw-Hill, 1964.
[36] Kawai T, Iguchi M, Tonami H. Kolloid Z 1967;221:28.
[37] Adams AM, Buckley CP, Jones DP. IMECE: Symposium on the Mechanics of Plastics and Plastic Composites, Annual Winter Meeting, 1995.